

Development and Test of a Two-Dimensional Stacked Terfenol-D Actuator With High Bandwidth and Large Stroke

Long Chen , Yuchuan Zhu , Jie Ling , *Member, IEEE*, and Zhao Feng 

Abstract—Smart material actuators (SMAs) can provide motion with high resolution and high bandwidth, but the output stroke is relatively small. Therefore, motion amplification mechanisms for SMAs have drawn considerable attentions in recent years. However, most of existing mechanisms realize the motion amplification at the expense of working bandwidth. To achieve large stroke and high bandwidth simultaneously, a novel two-dimensional stacked magnetostrictive actuator (TSMA) was developed and tested by adopting the magnetostrictive material, i.e., the Terfenol-D in this article. The U-shaped sleeves were employed to support the axial and radial two-dimensional stacking of three Terfenol-D rods. Then, an analytical model was established based on working principle of the TSMA, and a design of experiment analysis was carried out for the sensitivity study of the TSMA's key structural parameters. Next, the involved parameters of the established analytical model were obtained via system identification. Furthermore, several experimental tests of a fabricated prototype for the TSMA were carried out. The results show that the stroke of the proposed TSMA can reach $65 \mu\text{m}$. The displacement amplification ratio is achieved as 2.8 and the working bandwidth is kept as 500 Hz. This proves that the proposed structure can significantly increase the displacement with a little loss of bandwidth. Finally, a set of preliminary closed-loop tests using a traditional incremental proportion-integration-differentiation (PID) control were carried out to improve the motion precision. The closed-loop tracking results of 10–100 Hz sinusoid references show that the root-mean-square errors are less than 4% using a simple PID control alone.

Manuscript received December 3, 2020; revised March 21, 2021; accepted April 26, 2021. Date of publication May 14, 2021; date of current version August 13, 2021. Recommended by Technical Editor T. Shimono and Senior Editor X. Chen. This work was supported in part by the National Natural Science Foundation of China under Grant 51975275 and in part by the Postgraduate Research and Practice Innovation Program of Jiangsu Province, China, under Grant SJCX20_0066. (Corresponding authors: Yuchuan Zhu; Jie Ling.)

Long Chen, Yuchuan Zhu, and Jie Ling are with the College of Mechanical and Electrical Engineering, Nanjing University of Aeronautics and Astronautics, Nanjing 210016, China (e-mail: meelongchen@nuaa.edu.cn; meeyczhu@nuaa.edu.cn; meeijing@nuaa.edu.cn).

Zhao Feng is with the State Key Laboratory of Internet of Things for Smart City, University of Macau, Macau 999078, China, and also with the Faculty of Science and Technology, University of Macau, Macau 999078, China (e-mail: zhaofeng@um.edu.mo).

Color versions of one or more figures in this article are available at <https://doi.org/10.1109/TMECH.2021.3080395>.

Digital Object Identifier 10.1109/TMECH.2021.3080395

Index Terms—High bandwidth, motion amplification, smart material actuator, Terfenol-d, two-dimensional (2-D) magnetostrictive stack.

I. INTRODUCTION

RECENTLY, due to the advantages of high energy density and rapid response, smart materials have been widely used in many important fields such as robotics [1], [2], micromachining [3], optical instruments [4]–[6], and precision electric motors [7], etc. Magnetostrictive material is a kind of smart material, which can provide displacement under the excitation of an external magnetic field. Attributed to this noncontact driving method, the life and stability of magnetostrictive material are superior than other smart materials. Magnetostrictive actuators for high dynamic servo valves [8] and magnetostrictive electrohydraulic actuators for flap actuation [9], [10] usually have more rapid response and more reliable physical structure than a traditional one.

Nevertheless, a drawback of a magnetostrictive actuator is that the output displacement is normally less than 0.2% of its own length. In some application scenarios [11]–[13], the whole structure of the actuator should be compact with large stroke while its size should be small. For instance, a direct-drive servo valve requires submillimeter stroke of the spool [14]. The fuel injector actuator for combustion instabilities control also needs to have a submillimeter stroke [15].

The integration with amplification mechanisms is an effective method to increase the stroke. An amplification mechanism for a piezoelectric-based servo valve was developed by Karunanidhi *et al.* [16], where a maximum stroke of $135 \mu\text{m}$ is obtained and the corresponding bandwidth is 284 Hz (-90° phase). Chen *et al.* proposed a rhombus mechanism for motion amplification of piezoelectric actuators in [17]. The output displacement can reach $100 \mu\text{m}$. A three-stage motion amplification mechanism were developed by Tian *et al.* in [18], the maximum strokes of three axes are 177.33, 179.30, and $17.45 \mu\text{m}$, respectively. The first-two resonance frequencies are 102.69 and 106.86 Hz. Na *et al.* [19] investigated a reverse bridge type motion amplification mechanism. The maximum stroke is $880 \mu\text{m}$ and the resonance frequency is 69 Hz. Choi *et al.* [20] proposed a piezo-driven XY stage with a monolithic compliant parallel mechanism. The stroke is $\pm 110 \mu\text{m}$ in the x and y axes and the bandwidth is 20 Hz. Lai *et al.* [21] proposed a flexible motion amplification

mechanism. The travel range is $288.3 \mu\text{m}$, and the resonance frequency is 178 Hz.

Different from the indirect actuation method, which adopts amplification mechanisms, another method for motion amplification is the direct actuation with well-designed material structure. In our previous work, Li *et al.* [22] proposed a dual galferol rods-based actuator (DGA) with a bandwidth of 700 Hz. The displacement amplification is achieved through series connection of two galferol rods. But, due to a small magnetostrictive strain ratio of the galferol material [23], the maximum stroke of the DGA is only about $15 \mu\text{m}$.

However, looking into all the abovementioned designs, it can be observed directly that although the output displacement of some certain mechanisms can reach $100 \mu\text{m}$ or even larger, due to the usage of additional amplification mechanisms, none of these actuators has a bandwidth exceeding 300 Hz. In [18]–[20], compared with the bandwidth (about 1000 Hz) of smart materials themselves [24], the bandwidth of actuators has dropped by more than 70%. Thus, there is always a tradeoff between the large stroke and high bandwidth among existing SMAs. But, in some fields, SMAs need simultaneous large stroke and high bandwidth [25], [26]. Especially in the field of active combustion control of aeroengines, the actuator is usually required to have a bandwidth reach 500–1000 Hz and a submillimeter stroke simultaneously [27].

Inspired by the structure in our previous work in [22], a further improvement can be made by adopting materials with larger magnetostrictive strain ratios and modified structure. Terfenol-D is a kind of magnetostrictive material with an output up to two thousandths of its initial length [28]–[31]. Thus, to achieve the design goal of simultaneous large stroke and high bandwidth of a magnetostrictive actuator, a novel axial-radial two-dimensional stacked magnetostrictive actuator (TSMA) was developed in this work based on the principle of U-shaped sleeve motion amplification method by exploiting Terfenol-D. Compared with traditional magnetostrictive actuators of the same size, the output displacement of TSMA reaches $65 \mu\text{m}$, 2.8 times as much. Furthermore, compared with all the motion amplification actuators mentioned above, the bandwidth of the TSMA exceeds 500 Hz.

The rest of this article is organized as follows. The structure and working principle of the proposed TSMA is showed in Section II. Then, the analytical model of the TSMA is built in Section III. Section IV gives the elaborated process of the DOE analysis for the key parameters of the TSMA. Parameter identification and accuracy verification of the analytical model are carried out in Section V. Section VI presents the experiments on the fabricated prototype of the proposed TSMA and the analysis of the results. The effect of coil heating and load on the TSMA is discussed in Section VII. Finally, Section VIII concludes this article.

II. STRUCTURE AND WORKING PRINCIPLE OF THE TSMA

A. Motion Amplification Principle

The principle of the 2-D magnetostrictive stack is shown in Fig. 1. Two tubular and one cylindrical magnetostrictive rods are nested via two U-shaped sleeves. In the process of nesting of

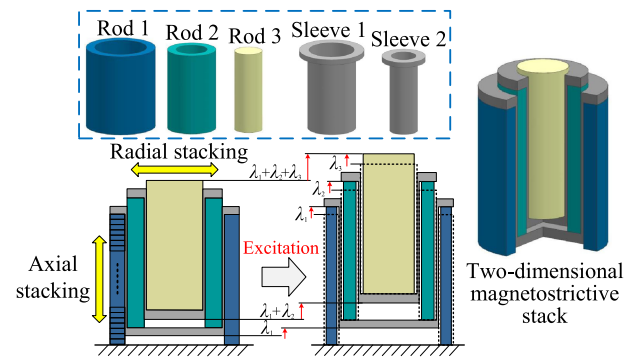


Fig. 1. Principle of the 2-D magnetostrictive stack. The sleeve material is stainless steel (SUS304). The black dotted frame is the original shape of Terfenol-D rods, λ_1 , λ_2 , and λ_3 respectively represent the output of rod 1 (tubular), rod 2 (tubular), and rod 3 (cylindrical). During the movement, the axial size of the Terfenol-D rod increases while the radial size decreases, and the volume remains unchanged.

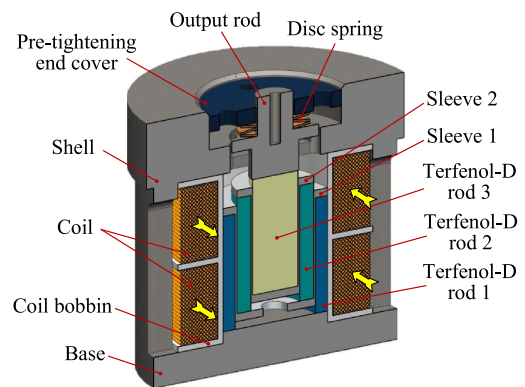


Fig. 2. Detailed structure of the TSMA. It is mainly composed of three parts: Magnetostrictive stack (Terfenol-D rod 1, Terfenol-D rod 2, Terfenol-D rod 3, Sleeve 1, and Sleeve 2), preload applying mechanism (disc spring, output rod, pretightening end cover, and shell) and electromagnetic excitation device (coil and coil bobbin). The yellow arrow represents the direction of excitation current. Two power amplifiers are employed to drive two coils at the same time to meet the drive power requirements of the TSMA performance test.

the magnetostrictive stack, both the axial and radial dimensions are simultaneously increasing.

In the TSMA, notations of magnetostrictive rods and sleeves are as follows: the rod (or sleeve) in the outermost layer is named as rod 1 (or sleeve 1), and it is named successively for the rod (or sleeve) 2, 3 from outside to inside. Under the action of an external excitation magnetic field, the three Terfenol-D rods extend at the same time, and the displacement of the lower Terfenol-D rods are transmitted upward through the sleeves, and finally superimposed into the total output displacement of the TSMA.

B. Structure of the TSMA

The structure of the proposed TSMA is shown in Fig. 2. The output performance of magnetostrictive materials can be greatly improved when there is a preload. In the TSMA preload applying device, the pretightening end cover compresses the disc spring to form a preload when tightened. The shell, the base, the output

rod, and the pretightening end cover are made of pure iron with extremely strong magnetic properties. The purpose is to produce a closed magnetic circuit inside the actuator, which is beneficial to improve the output performance of magnetostrictive materials.

Magnetostrictive materials have inherent frequency doubling effect, which can be eliminated by applying a constant bias magnetic field. Existing methods to eliminate frequency doubling effect included permanent magnet bias method and dc bias method [32]. In order to facilitate the performance test of the actuator, dc bias method was employed, thus the drive signal of the coil is a sinusoidal signal with a dc bias.

III. ANALYTICAL MODEL OF THE TSMA

The TSMA analytical model was built to describe the output hysteresis characteristics of the TSMA in this section.

A. Power Amplifier Voltage–Current Conversion Model

The power amplifier and its load coil winding can be approximately regarded as a first derivative element of an RC network and a second-order oscillation system, therefore, the voltage–current conversion process can be expressed by a second-order system, as shown in (1) [33]

$$\begin{aligned} G(s) &= \frac{k_U \omega_U^2 (1 + T_t s)}{s^2 + 2\xi_U \omega_U s + \omega_U^2} \\ &= \frac{k_U (1 + T_t s)}{\frac{1}{\omega_U^2} s^2 + 2\frac{\xi_U}{\omega_U} s + 1} = \frac{k_U (A s + 1)}{B s^2 + C s + 1} \end{aligned} \quad (1)$$

where k_U is the magnification, T_t is the time constant, ω_U and ξ_U , respectively, represent the natural frequency and damping ratio of the system.

B. Magnetization Model

The coil generates an excitation magnetic field under the action of current to drive the magnetostrictive rod. When considering the influence of eddy current, the magnetic field acting on a magnetostrictive rod is shown as (2) [22], [33]

$$H = \frac{NI}{k_f l (1 + \tau s)} = \frac{NI}{k_f l (1 + \mu_0 \mu_G (d_o^2 - d_i^2) s / 16 k_J \rho_G)} \quad (2)$$

where H is the magnetic intensity, N is the number of turns of the coil, I is the input current, k_f is the magnetic leakage coefficient, l is the length of a magnetostrictive rod, τ is the eddy current time constant, μ_0 is the vacuum permeability, μ_G is the relative permeability of the magnetostrictive rod, k_J is the electrical resistivity correction factor, ρ_G is the resistivity of the magnetostrictive rod, d_o and d_i is the outer and inner diameter of a magnetostrictive rod, respectively.

When a coil generates a driving magnetic field, the magnetostrictive rod is magnetized. So far, there are many magnetization models describing the magnetization process, mainly including phenomenological models such as Preisach model [34], physical models such as Jiles–Atherton model [35], etc. The Jiles–Atherton model (see Appendix B) is used in this article.

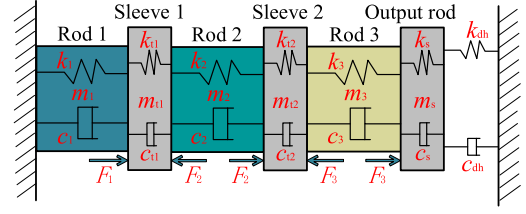


Fig. 3. Schematic of the multibody dynamics model. Terfenol-D rods become force sources when driven by a magnetic field. Sleeves and output rod act as elastic elements to transfer force and displacement.

C. Magnetostrictive Model

The magnetostrictive strain of a magnetostrictive rod mainly depends on three factors, including the saturation magnetostrictive strain of the magnetostrictive material, the magnetization intensity of the magnetostrictive material, and the preload applied to the magnetostrictive rod. The magnetostrictive strain can be expressed as (3) [36]

$$\begin{cases} \lambda = \left(1 + \frac{1}{2} \tanh \frac{2F}{F_s}\right) \lambda_s \frac{M^2}{M_s^2}, & F \leq F_s \\ \lambda = \left(1 - \frac{F - F_s}{F_{max}}\right) \left(1 + \frac{1}{2} \tanh \frac{2F}{F_s}\right) \lambda_s \frac{M^2}{M_s^2}, & F > F_s \end{cases} \quad (3)$$

where λ is the magnetostrictive strain, λ_s is the saturation magnetostrictive strain, F is the preload of a magnetostrictive rod, F_s is the optimal preload, M is the magnetization intensity, M_s is the saturation magnetization, and F_{max} is the maximum magnetostrictive force of the magnetostrictive rod, which can be calculated by

$$F_{max} = \frac{3}{2} \lambda_s E_G A_G \quad (4)$$

where E_G and A_G are the elastic modulus and the cross-sectional area of a magnetostrictive rod, respectively.

D. Development of the Multibody Dynamics Model

As shown in Fig. 3, the established dynamic equation can be expressed as

$$\begin{cases} m_1 \ddot{x}_1 = F_1 - k_1 x_1 - c_1 \dot{x}_1 - k_{t1} (x_1 - x_{t1}) - c_{t1} (\dot{x}_1 - \dot{x}_{t1}) \\ m_{t1} \ddot{x}_{t1} = -F_2 + k_{t1} (x_1 - x_{t1}) + c_{t1} (\dot{x}_1 - \dot{x}_{t1}) \\ \quad - k_2 (x_{t1} - x_2) - c_2 (\dot{x}_{t1} - \dot{x}_2) \\ m_2 \ddot{x}_2 = F_2 + k_2 (x_{t1} - x_2) + c_2 (\dot{x}_{t1} - \dot{x}_2) \\ \quad - k_{t2} (x_2 - x_{t2}) - c_{t2} (\dot{x}_2 - \dot{x}_{t2}) \\ m_{t2} \ddot{x}_{t2} = -F_3 + k_{t2} (x_2 - x_{t2}) + c_{t2} (\dot{x}_2 - \dot{x}_{t2}) \\ \quad - k_3 (x_{t2} - x_3) - c_3 (\dot{x}_{t2} - \dot{x}_3) \\ m_3 \ddot{x}_3 = F_3 + k_3 (x_{t2} - x_3) + c_3 (\dot{x}_{t2} - \dot{x}_3) \\ \quad - k_s (x_3 - x_s) - c_s (\dot{x}_3 - \dot{x}_s) \\ m_s \ddot{x}_s = k_s (x_3 - x_s) + c_s (\dot{x}_3 - \dot{x}_s) - k_{dh} x_s - c_{dh} \dot{x}_s \end{cases} \quad (5)$$

where x_1 , x_{t1} , x_2 , x_{t2} , x_3 , and x_s are the output displacements of the rod 1, the sleeve 1, the rod 2, the sleeve 2, the rod 3, and the output rod, respectively; m_1 , m_{t1} , m_2 , m_{t2} , m_3 , and m_s are the masses of the rod 1, the sleeve 1, the rod 2, the sleeve 2,

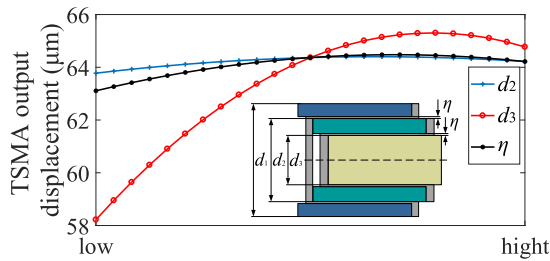


Fig. 4. DOE results analysis. Main Effect Plot, the degree to which key dimension parameters affect the TMSA output displacement. The horizontal axis represents the value range of each variable from low to high.

the rod 3, and the output rod, respectively; k_1 , k_{t1} , k_2 , k_{t2} , k_3 , k_s , and k_{dh} are the stiffness of the rod 1, the sleeve 1, the rod 2, the sleeve 2, the rod 3, the output rod and the disc spring, respectively; c_1 , c_{t1} , c_2 , c_{t2} , c_3 , c_s , and c_{dh} are the damping of the rod 1, the sleeve 1, the rod 2, the sleeve 2, the rod 3, the output rod, and the disc spring, respectively; F_1 , F_2 , and F_3 are the magnetostrictive force of the rod 1, the rod 2, and the rod 3, respectively.

IV. DOE ANALYSIS OF THE TSMA

A. Design Variables and Their Value Ranges

The 2-D magnetostrictive stack consists of three Terfenol-D rods and two U-shaped sleeves. The key dimensions include the outer diameter d_1 of the Terfenol-D rod 1, the outer diameter d_2 of the Terfenol-D rod 2, the outer diameter d_3 of the Terfenol-D rod 3, and the wall thickness η of the U-shaped sleeve. These dimensions directly affect the output performance of the TSMA. The analytical model of the TSMA was built in MATLAB/Simulink. Isight 2017 was employed to perform the DOE analysis.

Determined by the original Terfenol-D rod, the outer diameter d_1 of the rod 1 is 30 mm. So, the DOE experiment factors are d_2 , d_3 , and η . The experiment design goal is the maximum output displacement of the TSMA. The range of d_2 , d_3 , and η are 17–27 mm, 5–15 mm, and 0.1–0.5 mm, respectively.

B. Result Analysis

After effective analysis, the main effects plot for the TSMA output displacement was drawn as Fig. 4.

As shown in Fig. 4, the factor that has the greatest influence on the TSMA output displacement is the outer diameter d_3 of rod 3. When d_3 changed from 5 to 15 mm, the output displacement of TSMA changed by 10.85% and reach the maximum when d_3 is 12–14 mm. Thus, the rod 3 will be the top priority of the TSMA design. Therefore, the outer diameter d_3 of rod 3 was designed to be 13 mm. The dimensions of each Terfenol-D rods and sleeves are shown in Table I.

TABLE I
EXTERNAL DIMENSIONS OF THE TERFENOL-D RODS

Name	Outer diameter (m)	Inner diameter (m)	Length (m)
Rod 1	0.030	0.023	0.030
Sleeve 1	0.023	0.022	0.030
Rod 2	0.022	0.014	0.030
Sleeve 2	0.014	0.013	0.030
Rod 3	0.013	-	0.030

TABLE II
PARAMETERS OF THE TSMA DYNAMIC MODEL

Symbol	Unit	Value	Symbol	Unit	Value
m_1	g	81	k_{t2}	N·μm ⁻¹	160
k_1	N·μm ⁻¹	290	c_{t2}	N·s·m ⁻¹	2700
c_1	N·s·m ⁻¹	2900	m_3	g	37
m_{t1}	g	19	k_3	N·μm ⁻¹	130
k_{t1}	N·μm ⁻¹	280	c_3	N·s·m ⁻¹	880
c_{t1}	N·s·m ⁻¹	4600	m_s	g	22
m_2	g	63	k_s	N·μm ⁻¹	949
k_2	N·μm ⁻¹	220	c_s	N·s·m ⁻¹	9000
c_2	N·s·m ⁻¹	1510	k_{dh}	N·μm ⁻¹	0.8
m_{t2}	g	11	c_{dh}	N·s·m ⁻¹	2500

V. PARAMETER IDENTIFICATION AND ACCURACY VERIFICATION OF THE ANALYTICAL MODEL

A. Parameter Identification

MATLAB/Simulink was employed to identify parameters that cannot be measured or calculated in the TSMA analytical model, mainly including the parameter of the power amplifier transfer function (A , B and C), the damping of each part in the dynamic model (c_1 , c_{t1} , c_2 , c_{t2} , c_3 , c_s and c_{dh}), and the parameter of Jiles–Atherton model (a , α , c_r and k of rod 1 and rod 2). The target curve was obtained by experiment. Before starting the parameter identification, set the damping of each part to 0. The initial values of other parameters are determined based on the existing empirical values. Table II shows the parameters of the TSMA dynamic model in which the value of the mass (m_1 , m_{t1} , m_2 , m_{t2} , m_3 and m_s) and the stiffness (k_1 , k_{t1} , k_2 , k_{t2} , k_3 , k_s , and k_{dh}) were obtained through theoretical calculations and the damping were obtained through parameter identification.

The parameters of voltage–current conversion model obtained after parameter identification are as follows: $k_U = 1$, $A = 4.8e^{-4}$, $B = 2.5e^{-8}$, and $C = 6.4e^{-4}$.

For the Jiles–Atherton model, Terfenol-D rod 3 is cylindrical, its Jiles–Atherton model parameters have been obtained by our research group in previous studies [33]. But rod 2 and rod 3 are tubular, and their parameters are identified on the basis of rod 3 at low frequencies, as shown in Table III.

B. Comparison and Verification of the Magnetization Model

To verify the accuracy of the magnetostrictive rod's magnetization process described by the TSMA analytical model, a 2-D axisymmetric finite element model of the proposed TSMA was established. Both in the TSMA finite element model and the TSMA analytical model, the Jiles–Atherton model was used

TABLE III
PARAMETERS OF JILES-ATHERTON MODEL

Symbol	Unit	Rod1	Rod2	Rod3
M_s	$\text{kA}\cdot\text{m}^{-1}$	600	600	600
a	$\text{A}\cdot\text{m}^{-1}$	6512	10012	7012
α	---	-0.035	-0.01	-0.01
c_r	---	0.2	0.18	0.18
k	$\text{A}\cdot\text{m}^{-1}$	4000	5500	4283

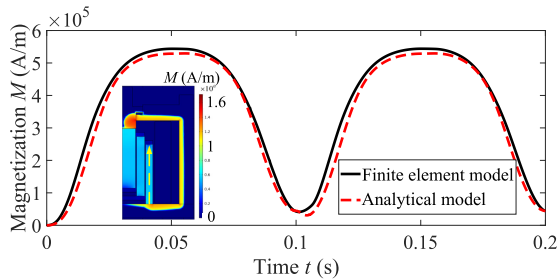


Fig. 5. Verification of the accuracy of magnetization process. The data extraction path of finite element model simulation results (along the yellow dotted line).

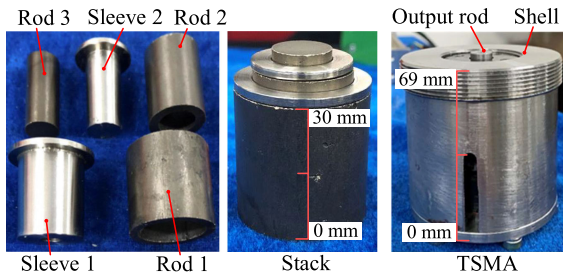


Fig. 6. Components of the TSMA prototype.

to describe the magnetization process of the magnetostrictive material. The magnetization intensity of Terfenol-D rod 1 under the excitation current of amplitude 12 A and frequency 10 Hz was calculated. It can be seen that the two curves in Fig. 5 have high coincidence.

VI. EXPERIMENTAL STUDY OF THE TSMA

In the experimental study, in order to meet the driving power requirements, the actuator has two independent coils. Two power amplifiers drive two coils simultaneously. The prototype of the TSMA is shown in Fig. 6.

A. Test Bench of the TSMA

As shown in Fig. 7, the output displacement of the TSMA was measured by an eddy current displacement sensor. The signal generator is responsible for the generation of sinusoidal excitation signal and amplifying it into a current signal through the power amplifier to directly drive the excitation coil. Single rod test and three rods nested (TSMA) test were carried out separately. Stainless steel rods were used to replace the other Terfenol-D rods when performing the single rod experiment.

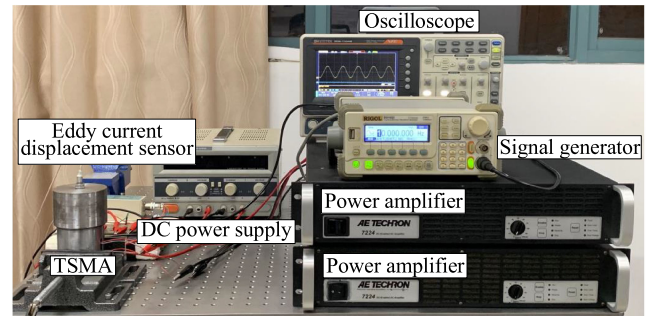
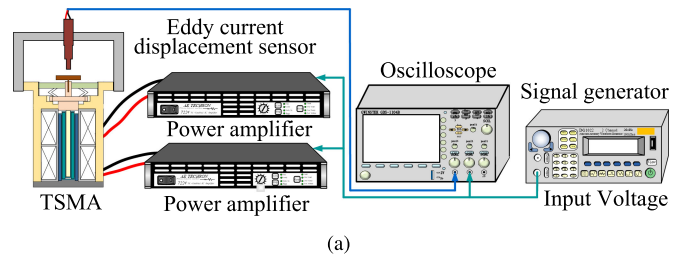


Fig. 7. Test bench of the TSMA. (a) Schematic of the test bench. (b) Physical photo of the test bench.

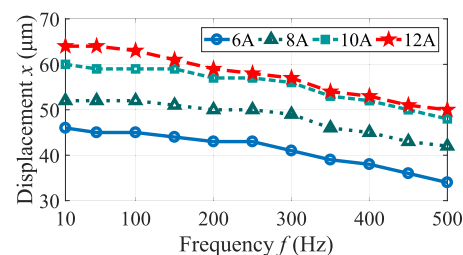
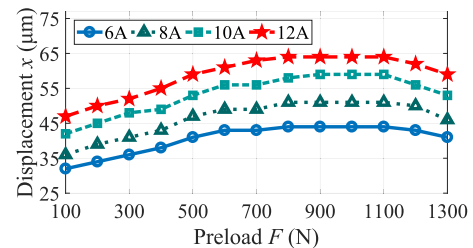


Fig. 8. Effect of preload and input current on the TSMA output displacement. (a) Preload. (b) Input current.

B. Performance Analysis of the TSMA

The driving signal is a sinusoidal signal with dc bias. For instance, 12 A refers to a sinusoidal input current with an amplitude of 0–12 A. Preload and input current are the main factors that affect the output performance of magnetostrictive materials. So their effects on the output performance of TSMA were analyzed first. As shown in Fig. 8(a), there is an optimal preload range between 800 and 1100 N for the TSMA to get a maximum output displacement of 65 μm. So the following experiments were performed under a preload of 900 N. It can be

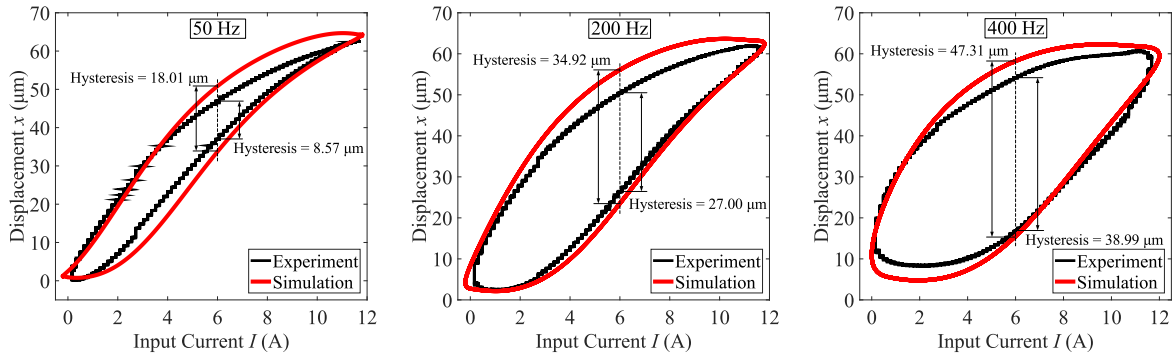
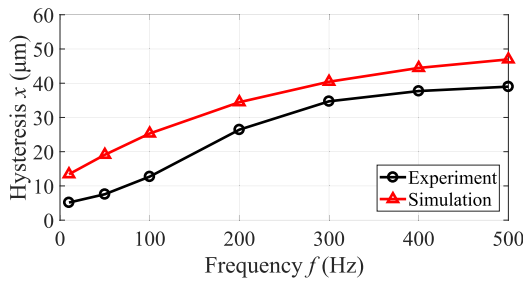
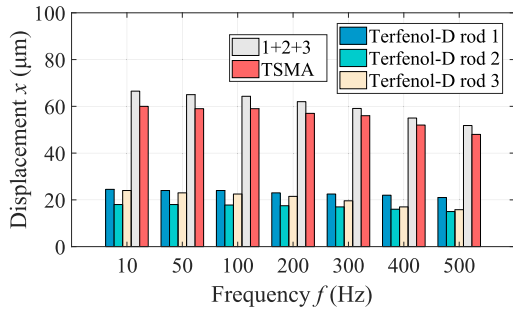


Fig. 9. Simulated and experimental hysteresis of the TSMA. Under 50, 200, and 400 Hz.



(a)



(b)

Fig. 10. Working bandwidth of the TSMA. (a) Effect of frequency on the hysteresis. (b) Effect of frequency on the output displacement. The excitation current amplitude is 10 A. The output displacement at 500 Hz is about 78% of that at 10 Hz.

seen from Fig. 8(b) that when the frequency exceeds 200 Hz, the output displacement at 12A no longer increases compared with that at 10 A. To study the high-frequency performance of the TSMA, the experiments were carried out under the maximum current of 12 A.

Fig. 9 show the simulation and experimental hysteresis comparisons of the TSMA, which indicates that the simulation can well predict the shape and trend of TSMA output hysteresis under different driving frequencies. As the driving frequency increases, the output displacement of the TSMA gradually attenuates, the hysteresis becomes more and more obvious. As shown in Fig. 10(a), the output hysteresis simulation result has the same trend as the experimental result. There is an error of 9 μm at different frequencies.

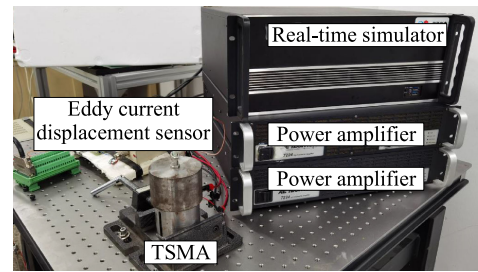


Fig. 11. TSMA closed-loop test platform.

The comparison of the output displacement of individual Terfenol-D rod and the TSMA under different driving frequencies are depicted in Fig. 10(b). Under the current amplitude of 10 A, the output displacement of rod 1 and rod 3 is about 22 μm , and the output displacement of rod 2 is about 17 μm . The total output displacement of the TSMA is about 60 μm , which is 90% of the sum of three rods tested separately, the loss is relatively small. Compared with a single rod, the displacement amplification ratio is achieved as 2.8. The output displacement at 500 Hz is about 78% of that at 10 Hz, which verify that the TSMA's working bandwidth can reach 500 Hz. The two-dimensional stacked structure has a significant amplification effect on the output displacement of the actuator, and the TSMA still has the characteristic of rapid response.

C. Closed-Loop Test of the TSMA

Through the above experimental analysis, it can be seen that the output nonlinearity of the TSMA becomes more and more serious as the driving frequency increases. In our previous work [33] and [37], detailed hysteresis modeling studies and inverse compensation studies for a magnetostrictive actuator have been carried out. Therefore, an incremental proportion-integration-differentiation (PID) closed-loop controller was further designed for the test of the TSMA's closed-loop output characteristics. In the TSMA closed-loop test platform, the output displacement of the TSMA was detected by an eddy current displacement sensor. Real-time simulator (Links-Box-03) with NI PCI6259 capture card was responsible for the signal acquisition and transmission. As shown in Fig. 11.

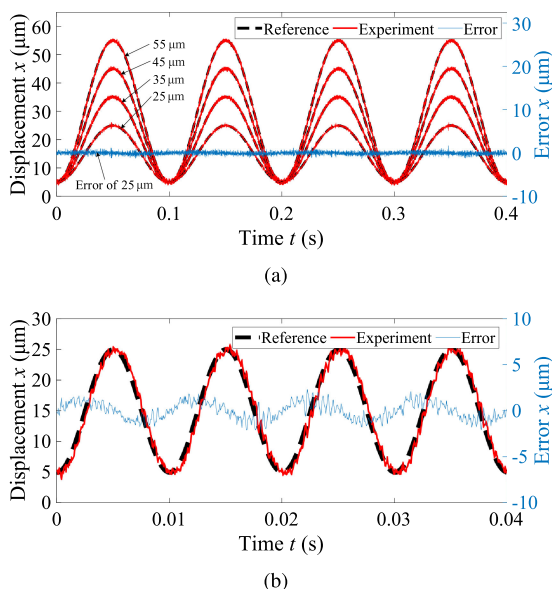


Fig. 12. Closed-loop test results of the TSMA. (a) 10 Hz. (b) 100 Hz. In the PID controller, $k_p = 7.7$, $k_i = 2$, and $k_d = 2$.

The closed-loop test results are shown in Fig. 12. Desired sinusoidal displacements with different amplitudes under different working frequencies were tracked. The root mean square error is $0.3377 \mu\text{m}$, $0.2973 \mu\text{m}$, $0.3026 \mu\text{m}$, $0.3290 \mu\text{m}$, and $0.9184 \mu\text{m}$ under the reference displacement amplitudes of $25 \mu\text{m}$, $35 \mu\text{m}$, $45 \mu\text{m}$, $55 \mu\text{m}$ at 10 Hz and $25 \mu\text{m}$ amplitude at 100 Hz, respectively. Thus, the TSMA can effectively track targets of sinusoidal displacement just using a PID controller.

VII. DISCUSSION

In this section, the effect of coil heating and load on the TSMA output performance is further analyzed.

A. Effect of Coil Heating

The TSMA transient thermal analysis finite element model was built, and the excitation current in the simulation is a sinusoidal signal with an amplitude of 10 A, a dc bias of 5 A and a frequency of 10 Hz. The coil generates heat after being energized and conducts the heat to the Terfenol-D rods. The temperature of each Terfenol-D rod was extracted for analysis, as shown in Fig. 13.

Since the rod 1 is close to the coil, its temperature rises more significantly than other rods. In the 10th and 20th second, the temperature of rod 1 increased by 1.36 and 5.42 °C, which cause thermal expansion of $0.53 \mu\text{m}$ and $2.1 \mu\text{m}$, respectively. Considering that the continuous working time of the TSMA in the experiment is usually less than 2 s, so the effect of heat during the experiment is relatively small and can be ignored.

B. Effect of Load

The analytical model was used to analyze the effect of load on the TSMA output performance. As shown in Fig. 14, a load

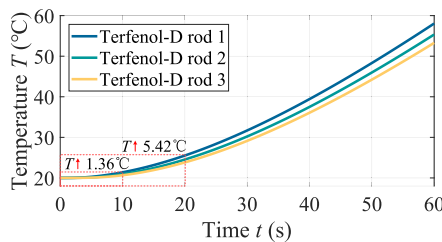


Fig. 13. Temperature rise curve of Terfenol-D rods. The coefficient of thermal expansion for Terfenol-D is $12.9 \times 10^{-6}/^\circ\text{C}$. This means that for a Terfenol-D rod with a length of 100 mm, the thermal expansion can reach $1.29 \mu\text{m}$ for every temperature increase of 1 °C.

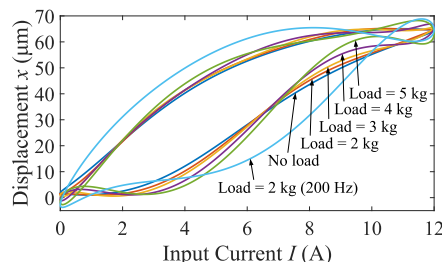


Fig. 14. Effect of mass load on the TSMA performance. Simulation under 100 Hz with different loads and 200 Hz with 2 kg load.

of 5 kg causes significant deformation of the TSMA output hysteresis at 100 Hz. When carrying a load, the output hysteresis of the TSMA has a tendency to rotate counterclockwise. For the same mass load, as the operating frequency increases, its impact on TSMA performance becomes greater.

VIII. CONCLUSION

In this article, a motion amplification actuator, named the two-dimensional stacked magnetostrictive actuator (TSMA), was developed based on Terfenol-D with high bandwidth and large stroke. The proposed TSMA can maximize the rapid response characteristics of smart materials, thanks to no additional mechanical deformation structure. An analytical model was established and a DOE analysis was carried out to investigate the sensitivity of some key structural parameters. Parameter identification and experiments were also conducted to test the achieved performances of the TSMA. According to the results, conclusions can be drawn as follows:

- 1) The outer diameter d_3 of the rod 3 has the greatest influence on the TSMA output displacement.
- 2) The analytical model can accurately describe the output hysteresis characteristics of the TSMA under different frequencies.
- 3) The stroke of the TSMA can reach $65 \mu\text{m}$ under an axial dimension of 69 mm. The displacement amplification ratio is achieved as 2.8 and the working bandwidth is kept as 500 Hz.
- 4) The closed-loop sinusoidal signal tracking experiment results indicate that the tracking root mean square error of

the TSMA under different frequencies and amplitudes are no more than $1 \mu\text{m}$ just using a traditional PID controller. Future works will seek to advanced control schemes to eliminate the effects of the nonlinearities so that to enhance the output performance of the proposed TSMA.

APPENDIX A

The fundamental characteristics of Terfenol-D is shown in Fig. 15.

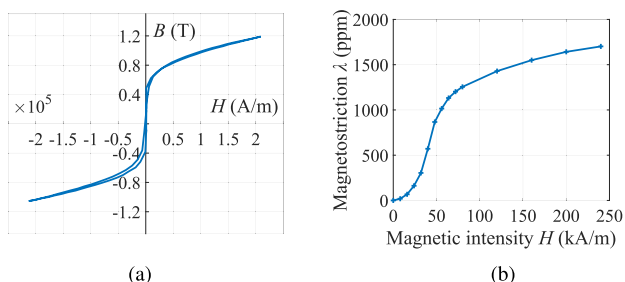


Fig. 15. Fundamental characteristics of Terfenol-D. (a) B - H curve. (b) H - λ curve, which were both provided by the manufacturer. where B is the magnetic induction, H is the magnetic intensity, and λ is the magnetostriction.

APPENDIX B

Jiles–Atherton model can be expressed by five equations:

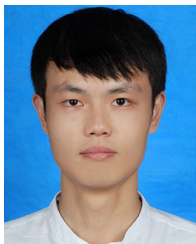
$$\begin{cases} H_e = H + \alpha M \\ M_{ir} = M_{an} - k\delta \left(\frac{dM_{ir}}{dH_e} \right) \\ M = M_r + M_{ir} \\ M_{an} = M_s \left[\coth \left(\frac{H_e}{a} \right) - \frac{a}{H_e} \right] \\ M_r = c_r (M_{an} - M_{ir}) \end{cases} \quad (6)$$

where M is the magnetization intensity of a magnetostrictive rod, M_s is the saturation magnetization, H_e is the effective magnetic field, M_r is the reversible value of magnetization, M_{ir} is the magnetization's irreversible value, M_{an} is an hysteretic value of magnetization, α is the magnetic domain interaction coefficient, c_r is the reversible coefficient, a is the shape coefficient of the magnetization curve without hysteresis, k is the pinning coefficient (the characteristic coefficient of hysteresis), and δ is the directional coefficient.

REFERENCES

- [1] A. G. Dharmawan, H. H. Hariri, G. S. Soh, S. Foong, and K. L. Wood, "Design, analysis, and characterization of a two-legged miniature robot with piezoelectric-driven four-bar linkage," *J. Mechanisms Robot.-Trans. ASME*, vol. 10, no. 2, 2018, Art. no. 021003.
- [2] M. Lok, E. F. Helbling, X. Zhang, R. Wood, D. Brooks, and G. Wei, "A low mass power electronics unit to drive piezoelectric actuators for flying microrobots," *IEEE Trans. Power Electron.*, vol. 33, no. 4, pp. 3180–3191, Apr. 2018.
- [3] Z. Wang, A. Witthauer, Q. Zou, G.-Y. Kim, and L. Faidley, "Control of a magnetostrictive-actuator-based micromachining system for optimal high-speed microforming process," *IEEE/ASME Trans. Mechatronics*, vol. 20, no. 3, pp. 1046–1055, Jun. 2015.
- [4] J. Ling, M. Rakoiondrabe, Z. Feng, M. Ming, and X. Xiao, "A robust resonant controller for high-speed scanning of nanopositioners: Design and implementation," *IEEE Trans. Control Syst. Technol.*, vol. 28, no. 3, pp. 1116–1123, May 2020.
- [5] Z. Feng, J. Ling, M. Ming, W. Y. Liang, K. K. Tan, and X. H. Xiao, "Signal-transformation-based repetitive control of spiral trajectory for piezoelectric nanopositioning stages," *IEEE/ASME Trans. Mechatronics*, vol. 25, no. 3, pp. 1634–1645, Jun. 2020.
- [6] J. Ling, Z. Feng, D. Zheng, J. Yang, H. Yu, and X. Xiao, "Robust adaptive motion tracking of piezoelectric actuated stages using online neural-network-based sliding mode control," *Mech. Syst. Signal Process.*, vol. 150, 2021, Art. no. 107235.
- [7] Z. Feng, W. Liang, J. Ling, X. Xiao, K. K. Tan, and T. H. Lee, "Integral terminal sliding-mode-based adaptive integral backstepping control for precision motion of a piezoelectric ultrasonic motor," *Mech. Syst. Signal Process.*, vol. 144, 2020, Art. no. 106856.
- [8] S. Karunanidhi and M. Singaperumal, "Design, analysis and simulation of magnetostrictive actuator and its application to high dynamic servo valve," *Sensors Actuators A, Phys.*, vol. 157, no. 2, pp. 185–197, 2010.
- [9] Y. C. Zhu, Z. Y. Wang, and S. S. Fei, "Development of a magnetostrictive material-based electro-hydrostatic actuator with an active rotary rectifying valve," *Proc. Inst. Mech. Eng. I, J. Syst. Control Eng.*, vol. 233, no. 8, pp. 994–1008, 2019.
- [10] Y. C. Zhu, X. L. Yang, and N. M. Wereley, "Theoretical and experimental investigations of a magnetostrictive electro-hydrostatic actuator," *Smart Mater. Struct.*, vol. 27, no. 10, 2018, Art. no. 105043.
- [11] J. Nam, H. Oh, and G. Jang, "Externally leveraged resonant piezoelectric actuator with fast response time for smart devices," *IEEE/ASME Trans. Mechatronics*, vol. 21, no. 6, pp. 2764–2772, Dec. 2016.
- [12] J. D. Ervin and D. Brei, "Recurve piezoelectric-strain-amplifying actuator architecture," *IEEE/ASME Trans. Mechatronics*, vol. 3, no. 4, pp. 293–301, Dec. 1998.
- [13] H. Zheng *et al.*, "Simulation and experiment of a diamond-type micro-displacement amplifier driven by piezoelectric actuator," *J. Eng.*, vol. 2020, no. 5, pp. 141–147, 2020.
- [14] G. P. Liu, Z. B. He, G. Bai, J. W. Zheng, J. T. Zhou, and M. Chang, "Modeling and experimental study of double-row bow-type micro-displacement amplifier for direct-drive servo valves," *Micromachines*, vol. 11, no. 3, 2020, Art. no. 312.
- [15] Y. Neumeier and B. T. zinn, "Experimental demonstration of active control of combustion instabilities using real-time modes observation and secondary fuel injection," *Symp. (Int.) Combustion*, vol. 26, no. 2, pp. 2811–2818, 1996.
- [16] S. Karunanidhi and M. Singaperumal, "Mathematical modelling and experimental characterization of a high dynamic servo valve integrated with piezoelectric actuator," *Proc. Inst. Mech. Engineers I, J. Syst. Control Eng.*, vol. 224, no. 14, pp. 419–435, 2010.
- [17] J. L. Chen, C. L. Zhang, M. L. Xu, Y. Y. Zi, and X. N. Zhang, "Rhombic micro-displacement amplifier for piezoelectric actuator and its linear and hybrid model," *Mech. Syst. Signal Process.*, vol. 50–51, pp. 580–593, 2015.
- [18] Y. Tian *et al.*, "A spatial deployable three-dof compliant nano-positioner with a three-stage motion amplification mechanism," *IEEE/ASME Trans. Mechatronics*, vol. 25, no. 3, pp. 1322–1334, Jun. 2020.
- [19] T. W. Na *et al.*, "Compact piezoelectric tripod manipulator based on a reverse bridge-type amplification mechanism," *Smart Mater. Struct.*, vol. 25, no. 9, 2016, Art. no. 095028.
- [20] K. B. Choi, J. Lee, G. Kim, H. Lim, S. Kwon, and S. C. Lee, "Design and analysis of a flexure-based parallel xy stage driven by differential piezo forces," *Int. J. Precis. Eng. Manuf.*, vol. 21, no. 8, pp. 1547–1561, 2020.
- [21] L. J. Lai and Z. N. Zhu, "Design, modeling and testing of a novel flexure-based displacement amplification mechanism," *Sensors Actuators A: Phys.*, vol. 266, pp. 122–129, 2017.
- [22] R. Q. Li, Y. C. Zhu, R. Wang, Y. Y. Li, and B. Niyomwungeri, "Design and analysis of a nested structure micro-displacement amplification mechanism for a galfenol-based actuator," *Smart Mater. Structures*, vol. 28, no. 9, 2019, Art. no. 095026.
- [23] A. E. Clark, M. Wun-Fogle, J. B. Restorff, and T. A. Lograsso, "Magnetostrictive properties of galfenol alloys under compressive stress," *Mater. Trans.*, vol. 43, no. 5, pp. 881–886, 2002.
- [24] G. Y. Yan, Y. B. Liu, and Z. H. Feng, "A dual-stage piezoelectric stack for high-speed and long-range actuation," *IEEE/ASME Trans. Mechatronics*, vol. 20, no. 5, pp. 2637–2641, 2015.
- [25] C. Zhou, G. L. Deng, J. H. Li, and J. A. Duan, "Flow channel influence of a collision-based piezoelectric jetting dispenser on jet performance," *Sensors*, vol. 18, no. 4, 2018, Art. no. 1270.

- [26] C. Zhou, J. Duan, G. Deng, and J. Li, "A novel high-speed jet dispenser driven by double piezoelectric stacks," *IEEE Trans. Ind. Electron.*, vol. 64, no. 1, pp. 412–419, Jan. 2017.
- [27] J. C. Delaat, K. J. Breisacher, J. R. Saus, and D. E. Paxson, "Active combustion control for aircraft gas turbine engines," in *Proc. 36th AIAA/ASME/SAE/ASEE Joint Propulsion Conf. Exhibit*, 2000, p. 3500.
- [28] Z. Yun *et al.*, "Significant non-bias-field magnetoelectric response and high output power in a novel combination based on terfenol-D and electrets," *IEEE Trans. Electron Devices*, vol. 67, no. 3, pp. 1323–1326, Mar. 2020.
- [29] W. Huang, C. Gao, Y. Li, and B. Wang, "Experimental and calculating analysis of high-frequency magnetic energy losses for terfenol-D magnetostrictive material," *IEEE Trans. Magn.*, vol. 54, no. 11, pp. 1–4, Nov. 2018.
- [30] L. Li, C. Zhang, B. Yan, L. Zhang, and X. Li, "Research of fast-response giant magnetostrictive actuator for space propulsion system," *IEEE Plasma Sci.*, vol. 39, no. 2, pp. 744–748, Feb. 2011.
- [31] Y. Sato and K. Shinohara, "Power-saving drive in 2-position control of giant-magnetostrictive actuator," *IEEE Trans. Magn.*, vol. 45, no. 10, pp. 4554–4557, Sep. 2009.
- [32] Z. Deng and M. J. Dapino, "Review of magnetostrictive materials for structural vibration control," *Smart Mater. Struct.*, vol. 27, no. 11, 2018, Art no. 113001.
- [33] Y. C. Zhu, X. L. Yang, and N. M. Wereley, "Research on hysteresis loop considering the prestress effect and electrical input dynamics for a giant magnetostrictive actuator," *Smart Mater. Struct.*, vol. 25, no. 8, 2016, Art no. 085030.
- [34] S. Hussain and D. A. Lowther, "An efficient implementation of the classical Preisach model," *IEEE Trans. Magn.*, vol. 54, no. 3, pp. 1–4, Mar. 2018.
- [35] D. C. Jiles, J. B. Thoenke, and M. K. Devine, "Numerical determination of hysteresis parameters for the modeling of magnetic properties using the theory of ferromagnetic hysteresis," *IEEE Trans. Magn.*, vol. 28, no. 1, pp. 27–35, Jan. 1992.
- [36] L. Sun and X. J. Zheng, "Numerical simulation on coupling behavior of terfenol-D rods," *Int. J. Solids Struct.*, vol. 43, no. 6, pp. 1613–1623, 2006.
- [37] Y. S. Li, Y. C. Zhu, H. T. Wu, and D. B. Tang, "Modeling and inverse compensation for giant magnetostrictive transducer applied in smart material electrohydrostatic actuator," *J. Intell. Mater. Syst. Struct.*, vol. 25, no. 3, pp. 378–388, 2013.



Long Chen received the B.S. degree from the School of Mechanical Engineering, Jiangsu University, Zhenjiang, China, in 2018, and he is currently working toward the Ph.D. degree with Nanjing University of Aeronautics and Astronautics, Nanjing, China, both in mechanical engineering.

His research interests include mechanical design and control of magnetostrictive actuators.



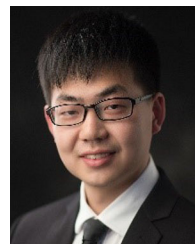
Yuchuan Zhu received the Ph.D. degree in mechanical engineering from Nanjing University of Science and Technology, Nanjing, China, in 2007.

He joined the Nanjing University of Aeronautics and Astronautics, Nanjing, China, in 2007, where he is currently a Full Professor with the Department of Mechanical and Electronic Engineering, College of Mechanical and Electrical Engineering. From 2014 to 2016, he was a Senior Visiting Scholar Fellow in the Department of Aeronautics and Astronautics, University of Maryland, USA. He has published more than 70 peer-reviewed papers in the areas of intelligent materials and structures, electro-hydraulic servo valves and electro-hydraulic actuators. His current research interests include intelligent materials and intelligent structures, advanced aviation hydraulics, electro-hydraulic servo valves and hydraulic simulation.



Jie Ling (Member, IEEE) received the B.S. and Ph.D. degrees from the School of Power and Mechanical Engineering, Wuhan University, Wuhan, China, in 2012 and 2018, respectively, both in mechanical engineering.

From August 2017 to November 2017, he was a visiting Ph.D. student with the Department of Automatic Control and Micro-Mechatronic Systems, FEMTO-st Institute, France. From January 2019 to January 2020, he was a Postdoctoral Research Fellow with the Department of Biomedical Engineering, National University of Singapore, Singapore. Since August 2020, he has been an Associate Research Fellow with the College of Mechanical and Electrical Engineering, Nanjing University of Aeronautics and Astronautics, Nanjing, China. His research interests include mechanical design and precision motion control of piezoelectric nanopositioning systems and micromanipulation robots.



Zhao Feng received the B.S. and Ph.D. degrees from the School of Power and Mechanical Engineering, Wuhan University, Wuhan, China, in 2014 and 2020, respectively, both in mechanical engineering.

From 2019 to 2020, he was also a visiting Ph.D. student with the Department of Electrical and Computer Engineering, National University of Singapore, Singapore. He is currently a Postdoctoral Fellow with the Faculty of Science and Technology, University of Macau, Macau, China.

His research interests include precision control, iterative learning control, nanopositioning, and robotics.